**Atmospheric
Chemistry
and Physics
Discussions**

Increased cloud activation potential of secondary organic aerosol for atmospheric mass loadings

S. M. King[1], T. Rosenoern[1], J. E. Shilling[1,*], Q. Chen[1], and S. T. Martin[1]

[1]School of Engineering and Applied Sciences & Department of Earth and Planetary Sciences, Harvard University, Cambridge, Massachusetts, USA
[*]now at: Pacific Northwest National Laboratory, Atmospheric Sciences and Global Change Division, Richland, WA 99352, USA

Correspondence to: S. T. Martin (scot_martin@harvard.edu)

S. M. King et al.

Abstract

The effect of organic particle mass loading from 1 to $\geq$100 µg m^{-3} on the cloud condensation nuclei (CCN) properties of mixed organic-sulfate particles was investigated in the Harvard Environmental Chamber. Mixed particles were produced by the condensation of organic molecules onto ammonium sulfate particles during the dark ozonolysis of α-pinene. A continuous-flow mode of the chamber provided stable conditions over long time periods, allowing for signal integration and hence increased measurement precision at low organic mass loadings representative of atmospheric conditions. CCN activity was measured at eight mass loadings for 80- and 100-nm particles grown on 50-nm sulfate seeds. A two-component (organic/sulfate) Köhler model, which included the particle heterogeneity arising from DMA size selection and from organic volume fraction for the selected 80- and 100-nm particles, was used to predict CCN activity. For organic mass loadings of 2.9 µg m^{-3} and greater, the observed activation curves were well predicted using a single set of physicochemical parameters for the organic component. For mass loadings of 1.74 µg m^{-3} and less, the observed CCN activity increased beyond predicted values using the same parameters, implying changed physicochemical properties of the organic component. Of possible changes in surface tension, effective molecular weight, and effective density, a sensitivity analysis implicated a decrease of up to 10% in surface tension at low mass loadings as the plausible dominant mechanism for the observed increase in CCN activity.

1 Introduction

Quantifying the potential of atmospheric particles to form cloud droplets is necessary for estimating the radiative forcing due to aerosol indirect effects, which at present have large uncertainties (IPCC, 2007). Recent models of these effects incorporate predictions of particle activation based on Köhler models (Lohmann and Feichter, 2005). Past laboratory investigations have shown that simple Köhler models agree well with mea-

sured cloud condensation nuclei (CCN) activity of inorganic particles (McFiggans et al., 2006). Atmospheric particles, however, also contain a significant mass fraction of complex organic compounds, and several laboratory studies using environmental chambers have been recently conducted to describe the CCN activation of secondary-organic-aerosol (SOA) particles produced by the oxidation of monoterpenes and sesquiterpenes (Hartz et al., 2005; VanReken et al., 2005; King et al., 2007; Prenni et al., 2007; Duplissy et al., 2008; Engelhart et al., 2008). Environmental chambers provide controlled surrogate atmospheres in which the formation of SOA can occur through the oxidation reactions of primary gaseous precursors. The results in these experiments suggest that the organic fraction of atmospheric particles could be more CCN active than previously thought.

The CCN activity of particles containing organic compounds may be enhanced by a reduction in surface tension from that of purely inorganic particles (Facchini et al., 1999; Svenningsson et al., 2006; Engelhart et al., 2008). King et al. (2007) reported on the CCN activity of internally mixed particles of ammonium sulfate and α-pinene SOA organic material and found that the critical supersaturations were well predicted using a two-component Köhler theory, specifically one component as ammonium sulfate and a second component representing the effective properties of the organic material. Agreement between the observations and the predictions of the Köhler model led to the conclusion that a surface tension of water was consistent with the observed activation of the mixed organic-sulfate particles. This finding was in agreement with several previous studies (Hegg et al., 2001; Ervens et al., 2005; Hartz et al., 2005) but in apparent disagreement with an assumption of a reduction in surface tension by particle-phase organic molecules (Facchini et al., 1999; Svenningsson et al., 2006; Engelhart et al., 2008).

The aforementioned studies of SOA CCN activity were performed in environmental chambers using biogenic volatile-organic-compound (VOC) precursor concentrations significantly above those commonly occurring in the atmosphere (Hartz et al., 2005; VanReken et al., 2005; King et al., 2007; Prenni et al., 2007; Duplissy et al., 2008;

Engelhart et al., 2008). For example, the lowest injected α-pinene concentrations for batch and continuous-flow chambers were 10 ppbv in Duplissy et al. (2008) and 24 ppbv in King et al. (2007), respectively. Given the dependency of the particle-phase composition of SOA on organic mass loading (Seinfeld and Pankow, 2003; Donahue et al., 2006; Shilling et al., 2008a), the CCN activity may also change. Although CCN activity at high SOA particle mass loadings did not find an effect of organic molecules on surface tension, such effects may emerge with the changed particle composition at low mass loadings representative of atmospheric concentrations. To explore this possibility, we undertook the studies described in this paper on the CCN activity of mixed organic-sulfate particles for variable mass loading. The CCN activity was investigated for organic particle mass loadings from 0.95 to $\geq$95.2 μg m^{-3}, a range across which considerable changes in the organic chemical composition can be expected based upon partitioning theory (Donahue et al., 2006; Shilling et al., 2008a).

2 Experimental

2.1 Overview

Inside the Harvard Environmental Chamber (HEC) (Fig. 1), organic molecules produced by the dark ozonolysis of α-pinene partition among the gas phase, the particle phase, and the walls. Initial condensation to the particle phase occurs on the surfaces of ammonium sulfate seed particles. Two types of environmental chambers have been described in previous reports, batch-mode chambers (Cocker et al., 2001b; Paulsen et al., 2005; Stanier et al., 2007) and continuous-flow chambers (Kleindienst et al., 1999). Continuous-flow operation is used for this study because conditions can be held stable over long time periods, allowing for more precise measurements through signal integration for low organic mass loadings representative of atmospheric conditions. For example, data in this study are collected over extended time periods (4 to 12 h) at organic loadings as low as 0.95 μg m^{-3}.

In a typical experiment, ammonium sulfate seed particles having an electric mobility equivalent to 50-nm spherical particles of +1 charge are selected using DMA_1 (Fig. 2). The transmitted aerosol includes both a mode of singly charged (+1) particles centered around a geometric diameter of 50 nm and a second mode of doubly charged (+2) particles centered around a geometric diameter of 73 nm. Organic molecules produced by the dark ozonolysis of α-pinene deposit onto these seed particles, leading to condensational growth. The rate of growth depends on the α-pinene concentration. The size distributions of the particles exiting the chamber are polydisperse, both because of several geometric modes of seed particles and because of the variability of particle residence times (i.e., growth times) in a continuously stirred tank reactor. From the particles exiting the chamber, 80- and 100-nm electric-mobility-equivalent particles are selected by DMA_2 for CCN analysis (Fig. 1). These particles contain a range of organic volume fractions, such as low fractions resulting from large (73 nm) seed particles that have short residence times and high fractions resulting from small (50 nm) seed particles that have long residence times. Additional heterogeneity arises from the transmission of multiply charged particles through DMA_2 (e.g., 80- and 120-nm geometric diameter for a setting of 80-nm mobility diameter on DMA_2). Interpretation of the CCN observations must account for these heterogeneities at a selected mobility diameter.

2.2 Chamber

A schematic diagram of the environmental chamber, including the associated injection systems and analysis instrumentation, is shown in Fig. 1. The constant-temperature chamber ($2.5 \times 2.5 \times 2.75$ m^3; Luwa Environmental Specialties) houses a flexible 4.7-m^3 bag ($1.7 \times 1.7 \times 1.7$ m^3), which is made from 0.05 mm (2 mil) PFA Teflon (Welch Fluorocarbon). The bag is suspended by a frame of stainless steel tubes, which also supports the bottom of the bag. The floor, the ceiling, and the walls of the chamber are covered by reflective aluminum sheets to maximize reflected light intensity. For wavelengths longer than 300 nm, the aluminum sheets have reflectivity better than 80%. Ultraviolet

irradiation is provided by forty-six 40-W Sylvania 350BL blacklights affixed to the walls. Except for bag cleaning, the blacklights are not used in this study.

The chamber is operated in a feedback-controlled continuous-flow mode (Kleindienst et al., 1999). Total flow, relative humidity, temperature, O_3 concentration, and NO_x
5   concentration are monitored and controlled by a PID circuit implemented in Labview. The inlet flow is balanced with the outlet flow by maintaining a constant overpressure in the bag of 30 mTorr using PID feedback to control a solenoid valve (Asco 8214). The pressure differential is measured by a manometer (Omega PX277). The temperature of the chamber is maintained within ±1°C between 15 and 40°C using an internal
10 conditioning plenum that distributes the air evenly through a perforated stainless steel ceiling. An RTD sensor measures the temperature outside of the bag, providing the feedback signal for temperature control.

Instrumentation for gas-phase measurements is summarized in Table 1. Relative humidity is monitored within the bag using a Rotronic Hygroclip SC05 sensor. Ozone
15 levels are measured using a UV absorption ozone analyzer (Teledyne 400E). NO and NO_2 concentrations are measured using a chemiluminescent NO_x analyzer (Teledyne 200E), which is calibrated using a 5 ppmv cylinder of NO (Airgas) diluted in N_2. No NO_x is introduced into the chamber for the dark ozonolysis experiments that constitute this study, and the measured levels remain below the detection limit of 1 ppbv.
20 Overall, the continuous-flow mode with feedback controls on total flow, relative humidity, temperature, O_3 concentration, and NO_x concentration maintains an approximately constant composition of gas- and particle-phase compounds during the course of an experiment.

The bag is periodically cleaned by turning off most flows and providing a continuous
25 flow of particle- and hydrocarbon-free air (40 L min^{-1}) having 600 ppbv O_3 while irradiating with UV lights at 40°C until the particle concentration is less than 1 cm^{-3} (typically 1–3 days).

2.3 Injection systems

The injection systems, consisting of solenoid valves and mass flow controllers regulated by Labview, are depicted in Fig. 2. An Aadco 737-14A Pure Air Generator removes hydrocarbons, H_2O, and NO_x from the house compressed air to provide a clean
5 dry flow having ambient concentrations of CO_2 and O_2 and a relative humidity of less than 1%. This air is used for several other subsystems, as indicated in Fig. 2. Ozone is synthesized by passing clean air around an ultraviolet lamp (Jelight 600). Two manifolds, located on opposite sides of the bag, provide multiple ports for injection and sampling lines. With the exception of Teflon lines used to sample O_3 and NO_x, the
10 injection and sampling lines are made from stainless steel.

A humid flow for adjusting relative humidity inside the bag is provided by proportional mixing of a near-saturation air flow with a dry-air flow. The near-saturation flow is obtained by bubbling dry air at a variable flow rate through $18\,M\Omega-cm$ water in a glass container. A HEPA filter (Pall 12144) is downstream of the bubbler to remove any
15 particles.

Dry seed particles are continuously generated from $(NH_4)_2SO_4$ solutions $(0.1\,g\,L^{-1})$ using a TSI 3076 atomizer, which is followed by a 160-cm silica gel diffusion dryer that has an exit relative humidity of less than 10%. The polydisperse particles are passed through a ^{85}Kr bipolar charger followed by a differential mobility analyzer (DMA_1, TSI
20 3071). For these experiments, DMA_1 is set to an electric mobility equivalent to 50-nm spherical particles of +1 charge and operated at a sheath-to-monodisperse flow ratio of 10:3. The exiting number concentration ranges from 5000 to $8000\,cm^{-3}$. Geometric diameters, as measured by an SMPS, include both a +1 mode at 50 nm and a significant +2 mode at 73 nm.

25 α-Pinene vapor is introduced using a syringe pump (New Era Pump Systems NE-1000) that continuously injects a mixture of α-pinene and 1-butanol (1:600 v/v, 1:1040 mole/mole) into a gently warmed glass bulb, which is flushed with clean dry air into the chamber. The pumping rate of the syringe determines the amount of α-

Cloud droplet activation of SOA at atmospheric mass loadings

S. M. King et al.

Title Page

Abstract	Introduction
Conclusions	References
Tables	Figures

|◄ | ►|
◄ | ►
Back | Close

Full Screen / Esc

Printer-friendly Version

Interactive Discussion

pinene available for reaction in the bag and thus affects the particle-phase organic mass loadings in the chamber. The pumping rate is slow enough that the hydrocarbon vapor is released into the glass bulb through evaporation from sessile drops on the tip of the syringe needle, rather than from released drops. 1-butanol serves as an OH scavenger.

The total flow rate through the bag is 21.1 sLpm, which includes 16 sLpm from the combined wet and dry clean air flows, 2 sLpm from the α-pinene/1-butanol flow, 3 sLpm from the seed flow, and up to 0.1 sLpm from the ozone flow. For 21.1 sLpm, the corresponding residence time in the chamber is approximately 3.4 h.

2.4 Particle characterization

The flow exiting the chamber first passes through a diffusion tube having an outer annulus filled with ozone destruction catalyst (Carus Chemical, Carulite 200). The flow is then split for simultaneous sampling by the particle instrumentation listed in Table 1 and shown in Fig. 1. A scanning mobility particle sizer (SMPS, TSI 3936) measures the electric-mobility-diameter size distribution. A condensation particle counter (CPC$_1$, TSI 3022) measures the total number concentration of the particles. An Aerodyne high-resolution time-of-flight aerosol mass spectrometer (HR-ToF-AMS) measures the organic and sulfate mass loadings (DeCarlo et al., 2006). A differential mobility analyzer (DMA$_2$) selects a monodisperse mobility-diameter fraction from the aerosol particles at a sheath-to-monodisperse flow ratio of 10:1.5, and this fraction is sampled simultaneously by a second CPC (CPC$_2$, TSI 3772) and a Droplet Measurement Technologies cloud condensation nucleus counter (CCNC, DMT CCN-2) (Roberts and Nenes, 2005; Lance et al., 2006). The activated fraction F_a is calculated as the number concentration of particles activating and growing to 1 µm or larger divided by the total number concentration counted by CPC$_2$. CPC$_2$ (TSI 3772) has a detector efficiency greater than 99% for particles larger than 30 nm. Calibration of the CCNC is performed with $(NH_4)_2SO_4$ (2007). Particle charge is re-equilibrated with a ^{85}Kr bipolar charger before sampling by the SMPS or DMA$_2$.

Full Screen / Esc

2.5 Protocols

In a typical experiment, the flows in the chamber are initiated by adjusting the relative humidity to 40% and the ozone concentration to 50 or 300 ppbv (cf. Table 2). The flow of sulfate seed particles is then initiated, which is followed by the flow of α-pinene mixed with 1-butanol. The α-pinene reacts with ozone inside the chamber, and the condensation of product molecules of sufficiently low vapor pressure ensues. These mixed organic-sulfate particles pass in the outlet flow from the chamber into several particle instruments for characterization. In the series of experiments constituting this study, the reaction conditions are held constant while the syringe pumping rate of the α-pinene and 1-butanol mixture are varied to adjust the resulting organic mass loading (Table 2). Data at one mass loading are typically collected for 2–4 days.

3 Theoretical approach

3.1 Köhler model

A two-component Köhler model assuming full solubility is used for calculating the critical supersaturation S^* for a particle of dry geometric diameter $D_{geo, dry}$. The saturation ratio s relative to a flat surface of liquid water is expressed as:

$$s = 1 + S/100 = n_w \left(n_w + \frac{\pi D_{geo, dry}^3}{6} \sum_{k \in \{AS, ORG\}} i_k \varepsilon_k V_{m,k}^{-1} \right)^{-1} \exp\left(\frac{4\sigma V_{m,w}}{RTD_{aq}} \right), \quad (1)$$

where S is the supersaturation (%), n_w is the number of moles of water, i_k is the van't Hoff factor of species k in solution, ε_k is the volume fraction of species k in the dry particle, $V_{m,k}$ is the molar volume of species k in the dry particle, σ is the surface tension, subscript w refers to pure water, R is the universal gas constant, T is the solution temperature, and D_{aq} is the aqueous particle diameter. Species k="AS" refers

to the ammonium sulfate seed, and species $k=$"ORG" refers to the organic component of the particle. The maximum of $S(D_{aq}; D_{\text{geo, dry}}, \varepsilon_{\text{ORG}})$ for variable D_{aq} corresponds to the critical supersaturation $S^*(D_{\text{geo, dry}}, \varepsilon_{\text{ORG}})$ that must be exceeded for activation. Equation (1) is derived in the supplementary material.

⁵   Table 3 shows the base-case values of the physicochemical parameters used in the evaluation of Eq. (1). King et al. (2007) established in a sensitivity study that the CCN activation of dark ozonolysis α-pinene SOA can be explained by a surface tension of water. That study also validated the assumption of full solubility of the SOA particle-phase organic component. CCN analysis, however, cannot individually constrain i_k

¹⁰ and $V_{m,k}$. For AS, these values are independently known, and the values are given in Table 3. For the organic component, our analysis assigns a formal value of unity to the van't Hoff factor i_{ORG}. The value of $148\,\text{cm}^3\,\text{mol}^{-1}$ for $V_{m,\text{ORG}}$ shown in Table 3 follows from (a) a density ρ_{ORG} of $1.2\pm0.1\,\text{g cm}^{-3}$ based on comparisons between the vacuum-aerodynamic size distribution and the electric-mobility size distribution for the highest

¹⁵ mass loading of this study (DeCarlo et al., 2004; Katrib et al., 2005; Kostenidou et al., 2007) and (b) a molecular weight M_{ORG} ($178\,\text{g mol}^{-1}$) that King et al. (2007) found as the optimal value to explain the CCN activity of dark ozonolysis α-pinene SOA organic material. The value for molar volume was calculated with ρ_{ORG} measured at the highest mass loading because ρ_{ORG} is independent of loading above $15.9\,\mu\text{g m}^{-3}$

²⁰ (Shilling et al., 2008a). For lower loadings, ρ_{ORG} increases, and these changes are incorporated in the present study as perturbations at low loadings to the base-case value of $V_{m,\text{ORG}}$. For comparison to our base-case value of $148\,\text{cm}^3\,\text{mol}^{-1}$, Hartz et al. (2005) reported a value of $146\,\text{cm}^3\,\text{mol}^{-1}$. In the framework of the κ-Köhler model of Petters and Kreidenweis (2007), the organic parameters of Table 3 correspond to

²⁵ $\kappa_{\text{ORG}}=0.12$ (Rose et al., 2007).

3.2 Calculated CCN activation curves

The activation curves correspond to the activated fraction F_a for increasing supersaturation S at a setpoint mobility diameter D_m. The activation curve $F_a(S; D_m)$ is expressed by Eq. (2):

$$F_a(S; D_m) = \frac{N_{CCNC}(S; D_m)}{N_{CPC}(D_m)} \tag{2}$$

for the number concentration of activated particles $N_{CCNC}(S; D_m)$ and the total number concentration $N_{CPC}(D_m)$.

The quantities $N_{CPC}(D_m)$ and $N_{CCNC}(S; D_m)$ can be calculated for the population of particles exiting the chamber. The population has a two-dimensional size/composition distribution $n_{chamber}(D_{geo}, \varepsilon_{ORG})$, where D_{geo} is the geometric diameter and ε_{ORG} is the volume fraction of organic material. The particles have a negligible water content when exiting the chamber and passing DMA$_2$ at 40% RH (Cocker et al., 2001a), implying both that $D_{geo}=D_{geo, dry}$ and that the organic volume fraction is balanced by ammonium sulfate (i.e., $\varepsilon_{ORG}+\varepsilon_{AS}=1$). For singly charged spherical particles, the mobility diameter and the geometric diameter are equal (Katrib et al., 2005).

The quantity $N_{CPC}(D_m)$ of Eq. (2) is calculated for 100% CPC detection efficiency using the following expression (Alofs and Balakumar, 1982; Collins et al., 2002):

$$N_{CPC}(D_m) = \int_0^\infty \sum_{j=-\infty}^{+\infty} \Omega(D_{geo}, j; D_m)\varphi(D_{geo}, j)n_{chamber}(D_{geo})dD_{geo}, \tag{3}$$

where Ω is the DMA fractional transmission at setpoint mobility diameter D_m for geometric diameter D_{geo} of a particle having charge j (Knutson and Whitby, 1975). The term φ is the fraction of particles of geometric diameter D_{geo} having charge j (Wiedensohler, 1988). The term $n_{chamber}(D_{geo})$ is the particle size distribution irrespective of organic volume fraction (i.e., the distribution obtained by the SMPS) and is expressed

as follows:

$$n_{\text{chamber}}(D_{\text{geo}}) = \int_0^1 n_{\text{chamber}}(\varepsilon_{\text{ORG}}; D_{\text{geo}}) d\varepsilon_{\text{ORG}}. \tag{4}$$

The concentration $N_{\text{CCNC}}(S; D_m)$ of particles activated as CCN at supersaturation S for the setpoint mobility diameter D_m in Eq. (2) is calculated as follows:

$$N_{\text{CCNC}}(S; D_m) =$$

$$\int_0^1 \int_0^\infty \sum_{j=-\infty}^{+\infty} \Omega(D_{\text{geo}}, j; D_m) \varphi(D_{\text{geo}}, j) n_{\text{chamber}}(D_{\text{geo}}, \varepsilon_{\text{ORG}}) \delta(D_{\text{geo}}, \varepsilon_{\text{ORG}}; S) dD_{\text{geo}} d\varepsilon_{\text{ORG}}, \tag{5}$$

where $\delta(D_{\text{geo}}, \varepsilon_{\text{ORG}}; S)$ takes a value of zero (not activated) for $S < S^*(D_{\text{geo}}, \varepsilon_{\text{ORG}})$ or unity (activated) for $S \geq S^*(D_{\text{geo}}, \varepsilon_{\text{ORG}})$, where $S^*(D_{\text{geo}}, \varepsilon_{\text{ORG}})$ is evaluated based on the maximum of Eq. (1).

Insight into $N_{\text{CCNC}}(S; D_m)$ and $F_a(S; D_m)$ can be obtained by consideration of the cumulative distribution function of organic volume fraction $\text{CDF}(\varepsilon_{\text{ORG}}; D_m)$ for a setpoint mobility diameter, which is calculated as follows:

$$\text{CDF}(\varepsilon_{\text{ORG}}; D_m) =$$

$$N_{\text{CPC}}^{-1}(D_m) \int_0^{\varepsilon_{\text{ORG}}} \int_0^\infty \sum_{j=-\infty}^{+\infty} \Omega(D_{\text{geo}}, j; D_m) \varphi(D_{\text{geo}}, j) n_{\text{chamber}}(D_{\text{geo}}, \varepsilon'_{\text{ORG}}) dD_{\text{geo}} d\varepsilon'_{\text{ORG}}, \tag{6}$$

where $\varepsilon'_{\text{ORG}}$ is a dummy variable of integration. Comparison of Eqs. (2), (5), and (6) shows that $F_a(S; D_m)$ corresponds $\text{CDF}(1; D_m)$ to when a weighting factor $\delta(D_{\text{geo}}, \varepsilon_{\text{ORG}}; S)$ is added to the integration.

3.3 Data analysis

Figure 3 illustrates graphically the CCN activation curve embodied in the model of Eqs. (2), (5), and (6). Panel a shows a cartoon of the geometric size distribution of

seed particles selected by DMA$_1$ for particles having an electric mobility equivalent to 50-nm spherical particles of +1 charge. The panel shows modes at 50- and 73-nm geometric diameter, which correspond to singly and doubly charged particles. The width of the mode arises from the DMA transmission function, though for illustration purposes the example in Fig. 3 is overly narrow compared to the actual distribution used in the model. Low-volatility products from the dark ozonolysis of α-pinene condense onto the seed particles of panel a, and the resulting volume partitioning among sulfate and organic material for increasing geometric diameter is illustrated in panel b. From the distribution shown in panel b, 80-nm (+1 charge) and 120-nm (+2 charge) geometric-diameter modes are selected by setting DMA$_2$ to an electric mobility equivalent to 80-nm spherical particles of +1 charge. Overall heterogeneity in the particles withdrawn from the chamber then includes four types: (1) 80-nm mode grown on the 50-nm mode of the seed particles, (2) 80-nm mode on 73-nm seeds, (3) 120-nm mode on 50-nm seeds, and (4) 120-nm mode on 73-nm seeds. These four types correspond to respective average organic volume fractions of 0.76, 0.24, 0.93, and 0.77. The resulting cumulative distribution function (CDF) of particles withdrawn from the chamber is illustrated in panel c (Eq. 6). The heterogeneity is further observed in the resulting CCN activation curve (Eq. 6) shown in panel d. The panel shows inflection points at the critical supersaturations corresponding to each particle type. The difference in critical supersaturation between 0.35% and 0.25% for the two organic volume fractions of 0.76 and 0.24 in the 80-nm mode is greater than the corresponding difference in critical supersaturation between 0.225% and 0.19% for the organic volume fractions of 0.93 and 0.77 for the 120-nm mode, emphasizing the importance of organic volume fraction on CCN activity.

For comparison to the approach embodied in Fig. 3, other treatments of multiply charged particles with CCN data analysis are presented in Rose et al. (2007) and Petters et al. (2007). Rose et al. subtract the activated fraction appearing as a plateau at lower supersaturations and corresponding to multiply charged particles (e.g., 120-nm mode on 73-nm seeds in panel c of Fig. 3) to renormalize the activation curve.

Petters et al. present an approach related to ours but differing in scanning of supersaturation rather than diameter. Our approach also extends that of Petters et al. (2007) by (1) incorporating variations of chemical composition in a forward Köhler model and (2) omitting a requirement of a definition of critical dry diameter or critical supersaturation from sigmoidal fits to observed data. Critical diameter or supersaturation is often defined as the diameter or supersaturation where 50% of the particles are CCN active (i.e., F_a=0.5), but this definition is frequently complicated by contributions from multiply charged particles (Petters et al., 2007). In the present study, this definition is also complicated by the chemical heterogeneity of the aerosol particles. Therefore, instead of finding a sigmoidal fit to the observed data, the observed CCN activation curves are modeled by the underlying physical and chemical properties of the particles.

4 Results and discussion

Typical size distributions of particles exiting the chamber are shown in Fig. 4. One distribution is shown for seed particles before injection of α-pinene, and three distributions are shown for organic-sulfate particles at three steady-state conditions that differ by the amount of added α-pinene. The latter distributions correspond to the lowest (0.95 µg m^{-3}), midrange (6.97 µg m^{-3}), and the highest ($\geq$95.2 µg m^{-3}) organic mass loadings of this study. As expected, particle diameter grows compared to the seed particles. The width of the distributions is also broader at higher loadings, representing the heterogeneity of particle residence times within the continuously stirred tank reactor.

Seinfeld et al. (2003) show that the size distribution $n_{chamber}(D_{geo})$ at steady-state in a continuous-flow chamber satisfies the relation:

$$\frac{d}{dD_{geo}}[I(D_{geo})n_{chamber}(D_{geo})] = -\left(\frac{1}{\tau} + \alpha\right) n_{chamber}(D_{geo}) + \frac{1}{\tau}n_{seed}(D_{geo}) \tag{7}$$

where τ is the mean residence time in the chamber, α is the size-dependent wall-loss coefficient, $n_{seed}(D_{geo})$ is the size distribution of the inflow seed particles, and $I(D_{geo})$ is

the diameter-dependent growth rate of the particles. For our experiment, the only unknown is $I(D_{geo})$. Least-squares optimization of Eq. (7) to the observed $n_{chamber}(D_{geo})$ gives $I(D_{geo})$. The results for $I(D_{geo})$ at the three loadings of Fig. 4 are shown in Fig. 5. As expected, the growth rates at higher organic loadings are faster compared to those at lower loadings, and the growth rates decrease with increasing particle size. As a check on the optimization (i.e., accuracy of $I(D_{geo})$), comparisons between the calculated $n_{chamber}(D_{geo})$ based on $I(D_{geo})$ and the measured $n_{chamber}(D_{geo})$ are provided in the supplementary material and show good agreement.

When optimizing, we impose that the diameter-dependent growth rate $I(D_{geo})$ must follow the form prescribed by Seinfeld et al. for a chemically nonreactive, semivolatile condensing species:

$$I(D_{geo}) = \sum_i \frac{\beta_i}{D_{geo} + \lambda_i} \tag{8}$$

where $i \in \{1, 2\}$. Although Seinfeld et al. interpret these values mechanistically (i.e., as two effective condensing species of relative vapor pressures), we do not mean to make these specific implications for this study. We only state that this form of the growth equation (i.e., Eq. 8 with $i \in \{1, 2\}$) has utility for formulating the growth-rate equation for use in modeling the steady-state size distribution (Eq. 7). Therefore, the possible covariances among β_i and λ_i are not considered in this study through a full sensitivity analysis for the optimization of Eq. (7).

From the aerosol exiting the chamber, particle modes of 80- and 100-nm equivalent diameter are selected using DMA_2 for CCN analysis. The number distributions of organic volume fractions $n_{chamber}(D_{geo}, \varepsilon_{ORG}; D_m)$ are modeled using the diameter-dependent growth rates and the observed seed particle size distribution. The resulting cumulative distribution functions $CDF(\varepsilon_{ORG}; D_m)$ for a mobility-equivalent particle mode of 100 nm are shown in Fig. 6 for organic particle mass loadings of 0.95, 6.97, and $\geq 95.2\,\mu g\,m^{-3}$.

The observed and the modeled CCN activation curves are shown in Fig. 7. The

Cloud droplet activation of SOA at atmospheric mass loadings

S. M. King et al.

modeled curves use Eq. (2) with the physicochemical Köhler parameters of Table 3 and incorporate $n_{chamber}(D_{geo}, \varepsilon_{ORG})$ through Eq. (5). The shoulders at lower supersaturations arise from the contribution of multiply charged particles, especially for the higher loadings for which the selected mobility-equivalent diameter is on the ascending branch of the geometric size distribution (cf. Fig. 4, $\geq 95.2\,\mu g\,m^{-3}$). In comparison, the shoulders for the lower loadings are small because of the reduced contribution by multiply charged particles when sampling the descending branch of the geometric size distribution.

Model calculations of mean ε_{ORG} demonstrate the necessity of considering the heterogeneity of the organic volume fraction for correct interpretation of the CCN activation curves. For example, the modeled mean ε_{ORG} for a mobility-equivalent particle mode of 100 nm at a loading of $\geq 95.2\,\mu g\,m^{-3}$ is 0.840. This value can be compared to 0.875 in a simpler calculation of organic volume fraction that assumes a homogenous seed particle geometric diameter of 50 nm for 100-nm geometric diameter particles exiting the chamber. At a loading of $6.97\,\mu g\,m^{-3}$, the mean ε_{ORG} shifts even further from 0.875 to 0.648. For the lowest loading of $0.95\,\mu g\,m^{-3}$, the modeled mean value is 0.546. Model calculations of mean ε_{ORG} are also verified through agreement with independent measurements of organic volume fraction using HR-ToF-AMS observations of size-dependent sulfate and organic mass loadings (King et al., 2007).

Apparent in Fig. 7 from the trend in root mean squared errors (RMSE) is an increase in observed CCN activity compared to the model for particle mass loadings of $1.74\,\mu g\,m^{-3}$ and less. The implication is that the physicochemical properties represented in Table 3 begin to change (e.g., a decrease in $V_{m,ORG}$ or in σ) for particle mass loadings of $1.74\,\mu g\,m^{-3}$ and less. Mass spectral characterization of the particles supports a change in chemical composition with lower loadings. For dark ozonolysis of α-pinene, Grieshop et al. (2007) found that m/z 44 increased from 4% for $500\,\mu g\,m^{-3}$, to 5% for $70\,\mu g\,m^{-3}$, and to 7% for $10\,\mu g\,m^{-3}$. In related studies in our chamber, we report in Shilling et al. (2008a) that m/z 44 increases from 7% for $37\,\mu g\,m^{-3}$, to 9% for $6\,\mu g\,m^{-3}$, and to 11% for $0.5\,\mu g\,m^{-3}$. Signal at m/z 44 includes fragments of oxo-

and di-carboxylic acids, and the increase for lower organic mass loadings plausibly indicates a corresponding increase in the mass fraction of these oxygenated, polar compounds, representing the types of organic molecules normally considered CCN active. Possible causes for the increase in oxygenated fraction at low loadings are
5 discussed in Shilling et al. (2008a).

A perturbation analysis is performed to explore how isolated changes in $V_{m,\mathrm{ORG}}$ or σ can improve the agreement between the observations and the model at the lowest studied mass loading (0.95 µg m^{-3}). Figure 8 presents the results. An optimized fit of the CCN activation curves at 80- and 100-nm equivalent mobility diameter is ob-
10 tained when the surface tension is decreased by 10% to 0.065 N m^{-1} while maintaining $V_{m,\mathrm{ORG}}$ at 148 cm^3 mol^{-1} (Fig. 8a). This decrease is comparable to that reported by Engelhart et al. (2008), who inferred a decrease in surface tension from the CCN activity of particles prepared from aqueous re-suspensions of filter samples of collected monoterpene SOA particle mass. Shading in Fig. 8b shows how perturbations
15 of ±25% to $V_{m,\mathrm{ORG}}$ affect the modeled CCN activation curves. This perturbation corresponds to the maximum observed increase in ρ_{ORG}, which is dependent upon loading lower than 15.9 µg m^{-3} and reaches its highest value in these experiments at a loading of 0.95 µg m^{-3} (Shilling et al., 2008a). The smaller sensitivity to $V_{m,\mathrm{ORG}}$ for supersaturations less than 0.3% may be due to the larger contribution of ammonium sulfate
20 (i.e., the organic fraction is small) at these supersaturations. Combined changes in the physicochemical properties are also possible. For example, a 25% change in $V_{m,\mathrm{ORG}}$ combined with a 7% decrease in surface tension leads to agreement between observed and calculated activation.

As an alternative to the resolved-properties approach of Eq. (1), Petters and Kreiden-
25 weis introduced a lumped-sum parameter κ (Petters and Kreidenweis, 2007). Agreement between the observed and modeled activation of Fig. 8 corresponds to an increase in κ_{ORG} to 0.16 at 0.95 µg m^{-3} compared to 0.12 at higher mass loadings. For further comparison, Prenni et al. (2007) and Engelhart et al. (2008) obtained ranges of κ values defined as 0.1±0.04 and 0.15±0.08, respectively, for several types of SOA

particles produced by dark ozonolysis in the absence of seed particles in batch-mode experiments. Precursors in those studies included α-pinene, β-pinene, limonene, and 3-carene. Additional variability in those studies may have occurred for any changes in CCN activity accompanying time-dependent SOA particle mass loading during the course of batch-mode experiments. We observed κ_{ORG} to shift by 0.04 when SOA particle mass loading decreased, all other factors held constant, for the dark ozonolysis of α-pinene.

In further regard to the resolved-properties approach of Eq. (1), the optimization suggests that a drop in surface tension of 10% explains the CCN observations at low SOA particle mass loadings. The overall drop in particle surface tension occurs even as the organic volume fraction decreases with loading (Fig. 6). A decrease in surface tension might be explained by increased quantities of surface-active organic molecules at low loadings. These molecules would be associated with the organic species having lower volatilities that preferentially condense into the particle phase at low loadings, and their effects would be present even as the total relative organic volume fraction decreases at low loadings because of their surface partitioning. At high loadings, the effect of these molecules on surface tension would diminish because of the dilution accompanying the condensation of the higher-volatility organic molecules. In addition to this explanation for the increase in CCN activity, changes in parameters of Eq. (1) aside from σ and $V_{m,ORG}$ might be possible. For example, the van't Hoff factor of the organic component i_{ORG} might deviate from unity. This factor could depend on the organic chemical composition, which varies with SOA particle mass loading. Mathematically, the effects of variability in i_{ORG} have the same form as those of $V_{m,ORG}$ so that significant changes beyond 25% variability would be required to match observations and data. Moreover, as in the case of $V_{m,ORG}$ the mismatch between modeled and observed activation at low supersaturations has low sensitivity to i_{ORG}. A reasonable conclusion is therefore to suggest that a decrease in surface tension is a plausible dominant mechanism for changes in CCN activity at low SOA particle mass loadings.

Supplementary material available

Equation (1) is derived in the supplementary material. Data shown in Fig. 7 are tabulated (Table S1). A comparison between the modeled and the observed steady-state size distributions is available (Fig. S1). See: http://www.atmos-chem-phys-discuss.net/9/1669/2009/acpd-9-1669-2009-supplement.pdf

References

Alofs, D. J. and Balakumar, P.: Inversion to obtain aerosol size distributions from measurements with a differential mobility analyzer, J. Aerosol Sci., 13, 513–527, 1982.

Cocker, D. R., Clegg, S. L., Flagan, R. C., and Seinfeld, J. H.: The effect of water on gas-particle partitioning of secondary organic aerosol. Part I: α-pinene/ozone system, Atmos. Environ., 35, 6049–6072, 2001a.

Cocker, D. R., Flagan, R. C., and Seinfeld, J. H.: State-of-the-art chamber facility for studying atmospheric aerosol chemistry, Environ. Sci. Technol., 35, 2594–2601, 2001b.

Collins, D. R., Flagan, R. C., and Seinfeld, J. H.: Improved inversion of scanning DMA data, Aerosol Sci. Technol., 36, 1–9, 2002.

DeCarlo, P. F., Slowik, J. G., Worsnop, D. R., Davidovits, P., and Jimenez, J. L.: Particle morphology and density characterization by combined mobility and aerodynamic diameter measurements. Part 1: Theory, Aerosol Sci. Technol., 38, 1185–1205, 2004.

DeCarlo, P. F., Kimmel, J. R., Trimborn, A., Northway, M. J., Jayne, J. T., Aiken, A. C., Gonin, M., Fuhrer, K., Horvath, T., Docherty, K. S., Worsnop, D. R., and Jimenez, J. L.: Field-deployable,

high-resolution, time-of-flight aerosol mass spectrometer, Anal. Chem., 78, 8281–8289, 2006.

Donahue, N. M., Robinson, A. L., Stanier, C. O., and Pandis, S. N.: Coupled partitioning, dilution, and chemical aging of semivolatile organics, Environ. Sci. Technol., 40, 2635–2643, 2006.

Duplissy, J., Gysel, M., Alfarra, M. R., Dommen, J., Metzger, A., Prevot, A. S. H., Weingart-ner, E., Laaksonen, A., Raatikainen, T., Good, N., Turner, S. F., McFiggans, G., and Bal-tensperger, U.: Cloud forming potential of secondary organic aerosol under near atmospheric conditions, Geophys. Res. Lett., 35, L03818, doi:03810.01029/02007GL031075, 2008.

Engelhart, G. J., Asa-Awuku, A., Nenes, A., and Pandis, S. N.: CCN activity and droplet growth kinetics of fresh and aged monoterpene secondary organic aerosol, Atmos. Chem. Phys., 8, 3937–3949, 2008,
http://www.atmos-chem-phys.net/8/3937/2008/.

Ervens, B., Feingold, G., and Kreidenweis, S. M.: Influence of water-soluble or-ganic carbon on cloud drop number concentration, J. Geophys. Res., 110, D18211, doi:18210.11029/12004JD005634, 2005.

Facchini, M. C., Mircea, M., Fuzzi, S., and Charlson, R. J.: Cloud albedo enhancement by surface-active organic solutes in growing droplets, Nature, 401, 257–259, 1999.

Grieshop, A. P., Donahue, N. M., and Robinson, A. L.: Is the gas-particle partitioning in alpha-pinene secondary organic aerosol reversible?, Geophys. Res. Lett., 34, L14810, doi:14810.11029/12007GL029987, 2007.

Hartz, K. E. H., Rosenoern, T., Ferchak, S. R., Raymond, T. M., Bilde, M., Donahue, N. M., and Pandis, S. N.: Cloud condensation nuclei activation of monoterpene and sesquiterpene sec-ondary organic aerosol, J. Geophys. Res., 110, D14208, doi:14210.11029/12004JD005754, 2005.

Hegg, D. A., Gao, S., Hoppel, W., Frick, G., Caffrey, P., Leaitch, W. R., Shantz, N., Ambrusko, J., and Albrechcinski, T.: Laboratory studies of the efficiency of selected organic aerosols as CCN, Atmos. Res., 58, 155–166, 2001.

IPCC (Intergovernmental Panel on Climate Change): Climate Change 2007: The Physical Science Basis, Cambridge University Press, 2007.

Katrib, Y., Martin, S. T., Rudich, Y., Davidovits, P., Jayne, J. T., and Worsnop, D. R.: Density changes of aerosol particles as a result of chemical reaction, Atmos. Chem. Phys., 5, 275–291, 2005,

http://www.atmos-chem-phys.net/5/275/2005/.

King, S. M., Rosenoern, T., Shilling, J. E., Chen, Q., and Martin, S. T.: Cloud condensation nucleus activity of secondary organic aerosol particles mixed with sulfate, Geophys. Res. Lett., 34, L24803, doi:24810.21029/22007GL030390, 2007.

Kleindienst, T. E., Smith, D. F., Li, W., Edney, E. O., Driscoll, D. J., Speer, R. E., and Weathers, W. S.: Secondary organic aerosol formation from the oxidation of aromatic hydrocarbons in the presence of dry submicron ammonium sulfate aerosol, Atmos. Environ., 33, 3669–3681, 1999.

Knutson, E. O. and Whitby, T. B.: Aerosol classification by electric mobility: Apparatus, theory, and applications, J. Aerosol Sci., 6, 443–451, 1975.

Kostenidou, E., Pathak, R. K., and Pandis, S. N.: An algorithm for the calculation of secondary organic aerosol density combining AMS and SMPS data, Aerosol Sci. Technol., 41, 1002–1010, 2007.

Lance, S., Medina, J., Smith, J. N., and Nenes, A.: Mapping the operation of the DMT Continuous Flow CCN counter, Aerosol Sci. Technol., 40, 242–254, 2006.

Lohmann, U. and Feichter, J.: Global indirect aerosol effects: a review, Atmos. Chem. Phys., 5, 715–737, 2005,
http://www.atmos-chem-phys.net/5/715/2005/.

McFiggans, G., Artaxo, P., Baltensperger, U., Coe, H., Facchini, M. C., Feingold, G., Fuzzi, S., Gysel, M., Laaksonen, A., Lohmann, U., Mentel, T. F., Murphy, D. M., O'Dowd, C. D., Snider, J. R., and Weingartner, E.: The effect of physical and chemical aerosol properties on warm cloud droplet activation, Atmos. Chem. Phys., 6, 2593–2649, 2006,
http://www.atmos-chem-phys.net/6/2593/2006/.

Paulsen, D., Dommen, J., Kalberer, M., Prevot, A. S. H., Richter, R., Sax, M., Steinbacher, M., Weingartner, E., and Baltensperger, U.: Secondary organic aerosol formation by irradiation of 1,3,5-trimethylbenzene-NO$_x$-H$_2$O in a new reaction chamber for atmospheric chemistry and physics, Environ. Sci. Technol., 39, 2668–2678, 2005.

Petters, M. D. and Kreidenweis, S. M.: A single parameter representation of hygroscopic growth and cloud condensation nucleus activity, Atmos. Chem. Phys., 7, 1961–1971, 2007,
http://www.atmos-chem-phys.net/7/1961/2007/.

Petters, M. D., Prenni, A. J., Kreidenweis, S. M., and DeMott, P. J.: On measuring the critical diameter of cloud condensation nuclei using mobility selected aerosol, Aerosol Sci. Technol., 41, 907–913, 2007.

Prenni, A. J., Petters, M. D., Kreidenweis, S. M., and DeMott, P. J.: Cloud droplet activation of secondary organic aerosol, J. Geophys. Res., 112, D10223, doi:10210.11029/12006JD007963, 2007.

Roberts, G. C. and Nenes, A.: A continuous-flow streamwise thermal-gradient CCN chamber for atmospheric measurements, Aerosol Sci. Technol., 39, 206–221, 2005.

Rose, D., Frank, G. P., Dusek, U., Gunthe, S. S., Andreae, M. O., and Poschl, U.: Calibration and measurement uncertainties of a continuous-flow cloud condensation nucleus counter (DMT-CCNC): CCN activation of ammonium sulfate and sodium chloride aerosol particles in theory and experiment, Atmos. Chem. Phys., 8, 1153–1179, 2008, http://www.atmos-chem-phys.net/8/1153/2008/.

Seinfeld, J. H., Kleindienst, T. E., Edney, E. O., and Cohen, J. B.: Aerosol growth in a steady-state, continuous flow chamber: Application to studies of secondary aerosol formation, Aerosol Sci. Technol., 37, 728–734, 2003.

Seinfeld, J. H. and Pankow, J. F.: Organic Atmospheric Particulate Material, Annu. Rev. Phys. Chem., 54, 121–140, 2003.

Shilling, J. E., King, S. M., Mochida, M., Worsnop, D. R., and Martin, S. T.: Mass spectral evidence that small changes in composition caused by oxidative aging processes alter aerosol CCN properties, J. Phys. Chem. A, 111, 3358–3368, 2007.

Shilling, J. E., Chen, Q., King, S. M., Rosenoern, T., Kroll, J. H., Worsnop, D. R., DeCarlo, P. F., Aiken, A. C., Sueper, D., Jimenez, J. L., and Martin, S. T.: Loading-dependent elemental composition of α-pinene SOA particles, Atmos. Chem. Phys. Discuss., 8, 15343–15373, 2008a, http://www.atmos-chem-phys-discuss.net/8/15343/2008/.

Shilling, J. E., Chen, Q., King, S. M., Rosenoern, T., Kroll, J. H., Worsnop, D. R., McKinney, K. A., and Martin, S. T.: Particle mass yield in secondary organic aerosol formed by the dark ozonolysis of α-pinene, Atmos. Chem. Phys., 8, 2073–2088, 2008b, http://www.atmos-chem-phys.net/8/2073/2008/.

Stanier, C. O., Pathak, R. K., and Pandis, S. N.: Measurements of the volatility of aerosols from α-pinene ozonolysis, Environ. Sci. Technol., 41, 2756–2763, 2007.

Svenningsson, B., Rissler, J., Swietlicki, E., Mircea, M., Bilde, M., Facchini, M. C., Decesari, S., Fuzzi, S., Zhou, J., Mønster, J., and Rosenoern, T.: Hygroscopic growth and critical supersaturations for mixed aerosol particles of inorganic and organic compounds of atmospheric relevance, Atmos. Chem. Phys., 6, 1937–1952, 2006,

Cloud droplet activation of SOA at atmospheric mass loadings

S. M. King et al.

Title Page

Abstract	Introduction
Conclusions	References
Tables	Figures

|◄ | ►|

◄ | ►

Back | Close

Full Screen / Esc

Printer-friendly Version

Interactive Discussion

http://www.atmos-chem-phys.net/6/1937/2006/.

VanReken, T. M., Ng, N. L., Flagan, R. C., and Seinfeld, J. H.: Cloud condensation nucleus activation properties of biogenic secondary organic aerosol, J. Geophys. Res., 110, D07206, doi:07210.01029/02004JD005465, 2005.

5   Wiedensohler, A.: An approximation of the bipolar charge distribution for particles in the sub-micron size range, J. Aerosol Sci., 19, 387–389, 1988.

Cloud droplet activation of SOA at atmospheric mass loadings

S. M. King et al.

Title Page

Abstract	Introduction
Conclusions	References
Tables	Figures

◄◄   ►►

◄   ►

Back   Close

Full Screen / Esc

Printer-friendly Version

Interactive Discussion

Table 1. Instrumentation outfitted for use with the environmental chamber.

Instrument	Measured parameter
Teledyne 400E ozone analyzer	O_3
Teledyne 200E NO_x analyzer	NO, NO_2
Rotronic Hygroclip SC05 sensor	relative humidity and temperature
Thermocouple type K	temperature
Ocean Optics USB2000 UV/VIS spectrometer	light spectrum
TSI 3025 condensation particle counter (CPC)	total particle number concentration
Scanning mobility particle sizer (TSI 3081 DMA and 3772 CPC)	number-weighted particle size distribution (0.01–1 µm)
TSI 3321 Aerodynamic Particle Sizer (APS)	number-weighted particle size distribution (0.5–20 µm)
Aerodyne high-resolution time-of-flight aerosol mass spectrometer (HR-ToF-AMS)	aerodynamic diameter and particle composition
Droplet Measurement Technologies cloud condensation nuclei counter (CCNC)	particle CCN properties

Table 2. Organic particle mass loadings and the corresponding ozone concentrations for the dark ozonolysis of α-pinene. The ozone levels are in both cases in stoichiometric excess, and the difference between the two concentrations was not observed to influence the CCN activity so long as similar mass loadings were compared (Shilling et al., 2008b).

Measurement date	Organic mass loading ($\mu g\,m^{-3}$)	O_3 (ppbv)
10 Jan 07	15.4	300
13 Jan 07	$\geq$95.2	300
17 Jan 07	2.90	300
24 Jan 07	6.97	300
6 Feb 07	1.24	300
12 Feb 07	0.95	300
23 Feb 07	1.74	50
27 Feb 07	5.01	50

Full Screen / Esc

Printer-friendly Version

Interactive Discussion

Table 3. Physical and chemical parameters appearing in Eq. (1) and used in the calculation of the CCN activation curves shown in Figs. 7 and 8 (King et al., 2007).

Parameter	Value
Surface tension, σ	$0.0725 \, \mathrm{N \, m^{-1}}$
Molar volume[*], $V_{m,\mathrm{AS}}$	$74.66 \, \mathrm{cm^3 \, mol^{-1}}$
van't Hoff factor of $(\mathrm{NH_4})_2\mathrm{SO_4}$, i_{AS}	2.2
Effective van't Hoff factor, i_{ORG}	1
Molar volume, $V_{m,\mathrm{ORG}}$	$148 \, \mathrm{cm^3 \, mol^{-1}}$

[*] $V_m = M/\rho$ where M is molecular weight and ρ is density.
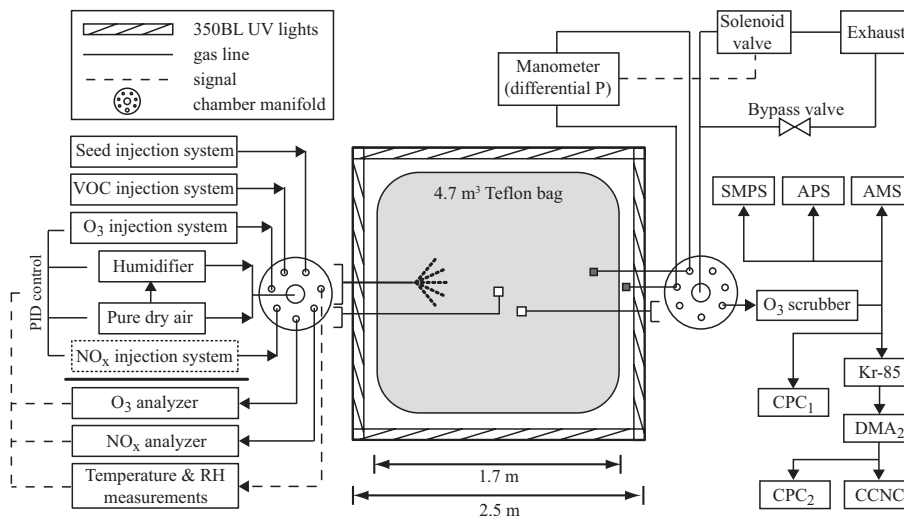
Fig. 1. Schematic diagram of the Harvard Environmental Chamber. There are injection systems for size-selected seed particles, VOC precursor, O_3, humidity, and NO_x. There are sampling and measurement systems for O_3, NO_x, temperature, relative humidity, particle size distribution (SMPS & APS), particle number concentration (CPC), particle chemistry (HR-ToF-AMS), and size-resolved CCNC activity (CPC & CCNC). Table 1 summarizes the instrumentation. Feedback controls maintain O_3, temperature, and relative humidity at fixed values. A differential pressure system balances outflow and inflow.
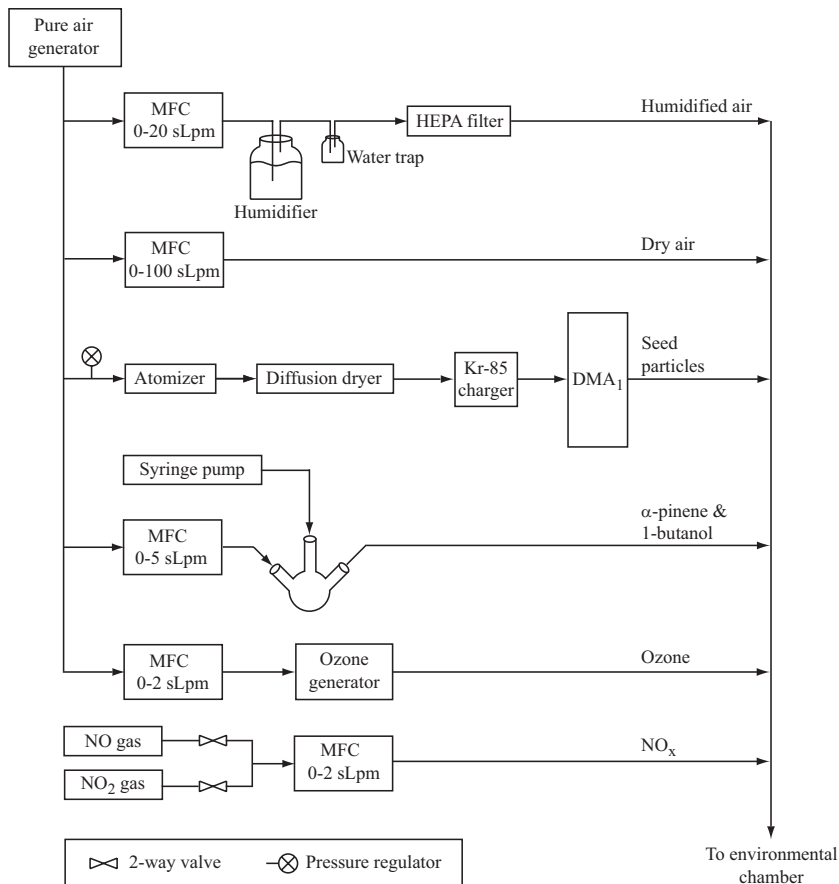
Fig. 2. Diagram of the injection systems for humidified air, dry air, size-selected seed particles, α-pinene as the precursor VOC (with 1-butanol as the OH scavenger), O_3, and NO_x. Mass flow controllers (MFC) are used to regulate flow in the injection systems, except in the case of the atomizer used for the seed particles.
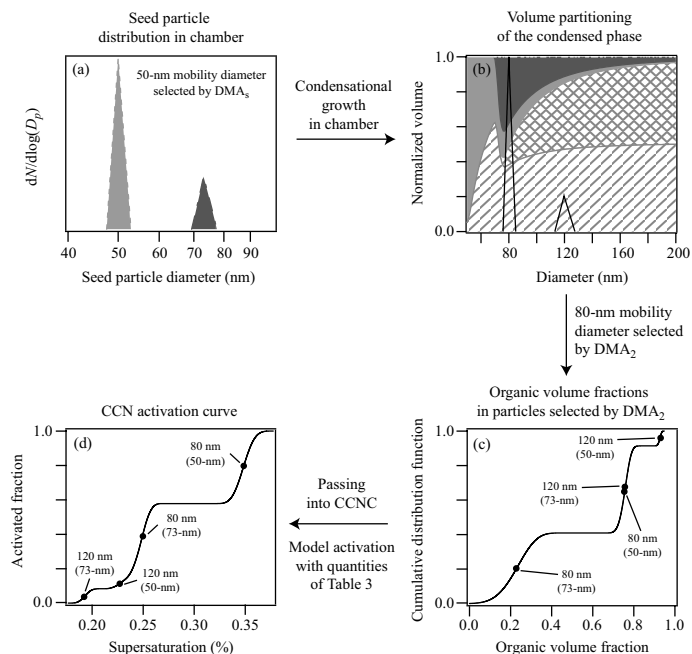
Fig. 3. Illustration of the experimental design and the model analysis. **(a)** Seed-particle geometric-size distribution for an electric-mobility diameter equivalent to 50-nm spherical particles having a +1 charge selected by DMA$_1$. Light and dark gray represent singly and doubly charged particles, respectively. Although the actual model uses observed seed size distributions that have more highly charged particles and broader transmission functions, the illustration is simplified for presentation. **(b)** Volume partitioning for increasing geometric diameter between sulfate and organic particle-phase material: (light gray) the sulfate volume fraction arising from the 50-nm mode of seed particles, (dark gray) the sulfate volume fraction due to the 73-nm mode, (hashing) the volume fraction of organic material condensed onto the 50-nm seeds, and (crossed pattern) the volume fraction of organic material condensed onto the 73-nm seeds. Also shown are the geometric-diameter transmission windows of 80-nm mobility diameter for singly and doubly charged particles. The growth rate used in the illustration corresponds to the lowest loading of the experiments (i.e., 0.95 µg m^{-3}). **(c)** Cumulative distribution function (CDF) of organic volume fraction for particles of 80-nm mobility diameter selected by DMA$_2$. See main text for further description of the four particle compositions. **(d)** CCN activation curve for particles corresponding to panel (c).
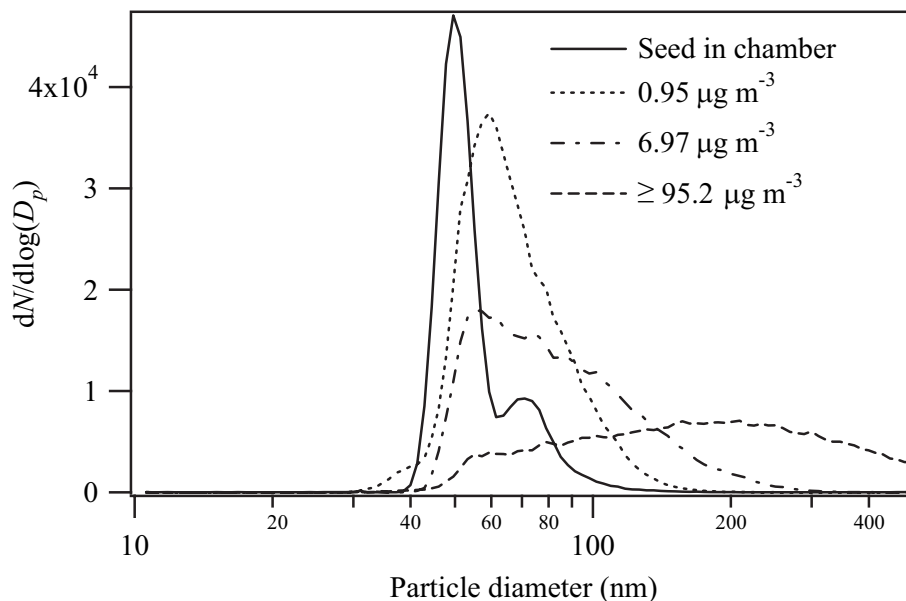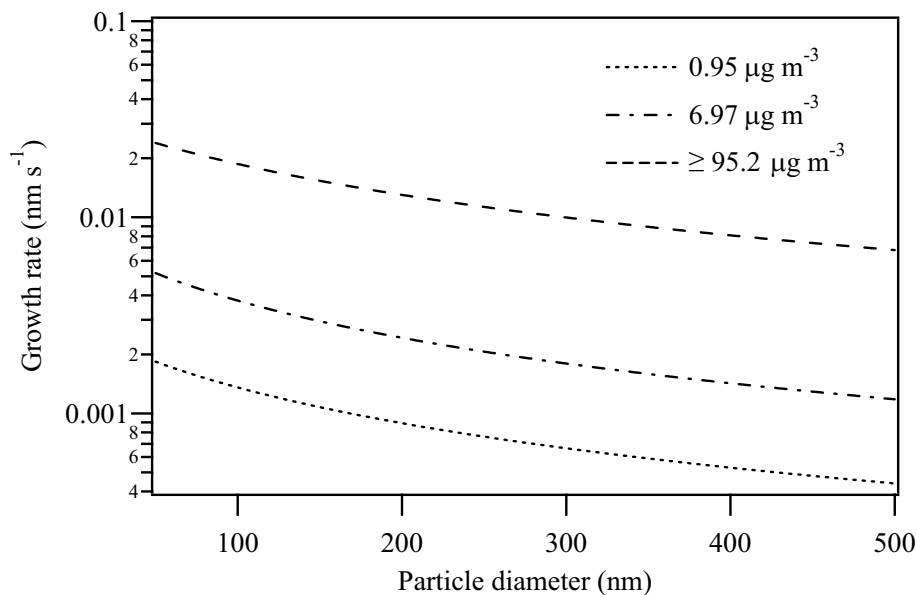
Fig. 4. Steady-state number size distributions measured by the SMPS. The solid line shows observations corresponding to the sulfate seed particles (i.e., no VOC injection) selected by DMA$_1$ for an electric mobility diameter equivalent to 50-nm spherical particles of +1 charge and then recharged in a neutralizer prior to entering the SMPS. The mode at 73 nm arises from particles doubly charged in DMA$_1$ but singly charged in the SMPS. The dashed lines show the size distributions after coating by organic material for three different mass loadings that represent the range of those used in this study. The SOA was prepared by the dark ozonolysis of α-pinene at 25°C and 40% relative humidity.

Fig. 5. Steady-state diameter-dependent growth rates for the three mass loadings shown in Fig. 4. These results are calculated from a best-fit model of the steady-state size distributions using the formulation of Seinfeld et al. (2003).
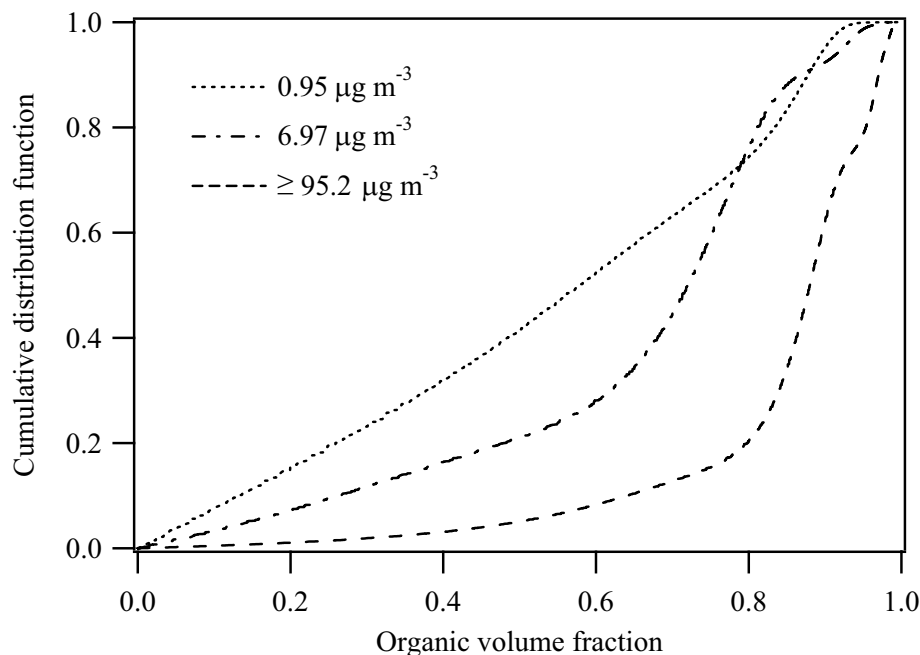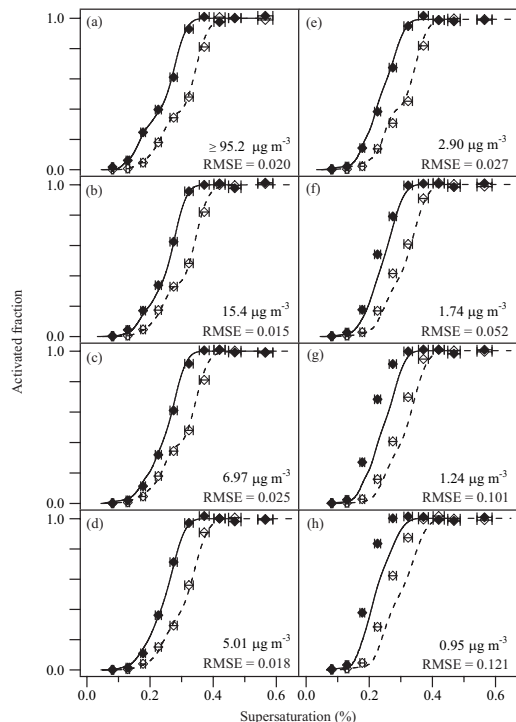
Fig. 6. Cumulative distribution functions of organic volume fraction ε_{ORG} for particles having an electric mobility diameter equivalent to 100-nm spherical particles of +1 charge and selected by DMA2 from the three size distributions of Fig. 4. These curves are calculated using the best-fit growth rates of Fig. 5.

Fig. 7. Observed and modeled CCN activated fraction for increasing supersaturation. Observed data were collected for several hours and averaged. Panels show results from 0.95 to $\geq 95.2\,\mu g\,m^{-3}$ organic particle mass loading. Solid symbols represent results for particles passing DMA_2 when set to an equivalent electric-mobility diameter of 100 nm for spherical particles of +1 charge. Open symbols represent results for 80-nm electric-mobility-equivalent particles. The solid and dashed lines are the modeled CCN activation curves for these two mobility diameters (Fig. 3). Physical and chemical properties used in the model are provided in Table 3. The shown root mean squared errors (RMSE) are for the observations compared to models when summed for both particle sizes.
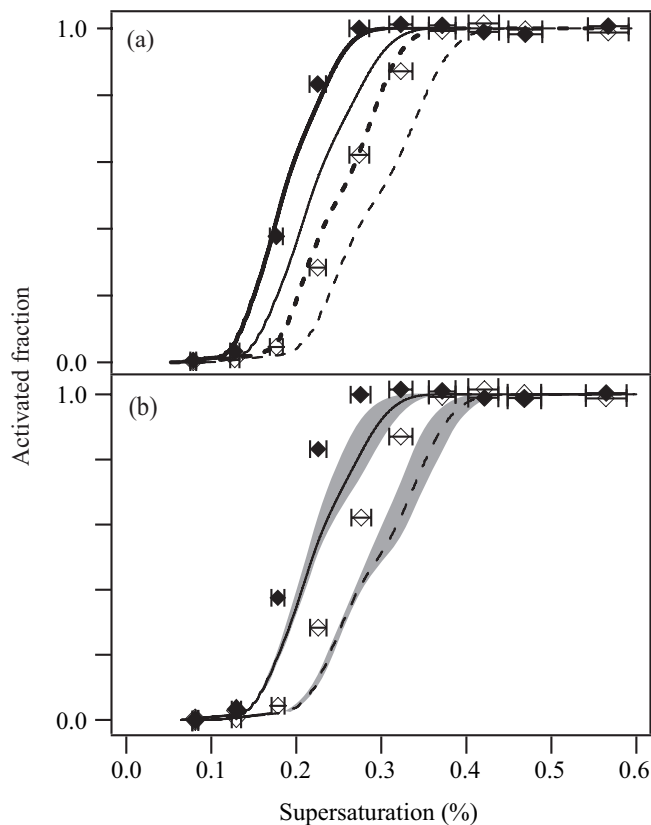
Fig. 8. Sensitivity of modeled activation curves at the lowest organic particle mass loading of 0.95 μg m^{-3} to **(a)** perturbation of −10% in surface tension σ and **(b)** perturbations of ±25% in molar volume $V_{m,\text{ORG}}$ compared to the values given in Table 3. Legend: symbols and thin lines are as in Fig. 7. The bold lines in panel (a) represent the curves after perturbation of −10% in σ. The gray region in panel (b) represents the results of perturbations of ±25%.